

Developing Ultrafine Twinned Microstructure Enabled Excellent Strength–Ductility Synergy in Mg–Al–Zn Alloy by Submerged Friction Stir Processing



TAO SUN, FUJUN CAO, JINPENG HU, YIFU SHEN, XIAOYANG QU, and WEI XU

Traditional multi-pass friction stir processing (FSP) can homogenize the microstructure and enhance the mechanical properties of magnesium alloy, but the thermal cycle between adjacent passes will lead to a large heat-affected zone (HAZ), which will cause the inability to create large high-performance areas. In this paper, magnesium alloy with ultrafine grains was correctly prepared by multi-pass submerged FSP (SFSP), and a large number of fine tensile twins were introduced into the stirring zone (SZ). The microstructure and properties of the SZ under different processing conditions were characterized by scanning electron microscopy, X-ray diffraction, electron backscatter diffraction, and transmission electron microscopy. The effects of microstructure and substructure on mechanical properties were systematically studied. The results show that the thermal cycle was seriously weakened and the HAZ was significantly reduced compared with air-cooling FSP (AFSP). In addition, SFSP led to more uniform distribution of second-phase particles and introduced high-density dislocations, while the dislocation density decreased after AFSP. Although the high dislocation density tended to lead to plasticity loss, this unique microstructure allows the material to achieve satisfactory mechanical properties.

<https://doi.org/10.1007/s11661-023-07201-x>

© The Minerals, Metals & Materials Society and ASM International 2023

I. INTRODUCTION

CURRENTLY, magnesium alloys, as the lightest structural alloys, have received extensive attention around the world due to their high strength-to-weight ratio and recyclability.^[1] They have great application potential to improve energy efficiency in aerospace, high-speed rail, and automotive. Unfortunately, dislocation is dominated by basal plane slip during plastic deformation at room temperature due to the hexagonal close-packed (HCP) crystal structure, which results in unsatisfactory comprehensive mechanical properties. Furthermore, poor corrosion resistance is also a key factor restricting the application of magnesium alloys.

For more than two decades, a large amount of research has been devoted to improving the strength, ductility, or corrosion resistance of magnesium alloys. Xu *et al.*^[2] produced a Mg–Li–Al alloy with ultra-high strength and good corrosion resistance by strengthening the processing technology and composition design. Wan *et al.*^[3] prepared nanocrystalline high-strength magnesium alloys by a conventional industrial method of rotary swagging. Jung *et al.*^[4] pointed out that rare earth elements can change the stacking fault energy of Mg and effectively hinder the movement of dislocations, thereby significantly improving the strength of magnesium alloys. Homma *et al.*^[5] achieved successfully magnesium alloy with high strength plasticity synergistic coordination by using the ingot metallurgical process combining hot extrusion and aging. They demonstrated that the high strength is the result of fine precipitates from aging and dynamic precipitation at the grain boundaries (GBs) of dynamically recrystallized grains. These reports provide a lot of theoretical support for the application of magnesium alloys. Although these processes can efficiently optimize the properties of magnesium alloys, their high cost and complex process restrict inevitably their industrial applications. In addition, these processes are prone to lead to serious grain growth

TAO SUN, FUJUN CAO, JINPENG HU, and YIFU SHEN are with the College of Materials Science and Technology, Nanjing University of Aeronautics and Astronautics, 29 Jiangjun Road, Nanjing 210016, P.R. China. Contact e-mail: yfshen_nuaa@hotmail.com XIAOYANG QU, and WEI XU are with the Technology Research Institute of Nanjing Chenguang Group Co LTD, No. 1. Zhengxue Road, Nanjing 210006, P.R. China.

Manuscript submitted April 22, 2023; accepted September 7, 2023.
Article published online September 22, 2023

and brittle intermetallic compounds (IMCs) precipitation, and other metallurgical problems.

Friction stir processing (FSP), as a severe plastic deformation (SPD) technique, was developed based on friction stir welding (FSW). The FSPed materials usually do not undergo melting and solidification processes.^[6] Therefore, it naturally shows great advantages in obtaining high-level magnesium alloys due to their inherently superior ability to alleviate the above-mentioned problems. Recently, Liu *et al.*^[7] investigated the grain structure of the SZ of AZ31 after FSP and proved that there was significant grain refinement and mechanical property enhancement in the SZ. Liu *et al.*^[8] also proved the phenomenon. Liu *et al.*^[9] found that the corrosion resistance of FSPed magnesium alloys was significantly strengthened due to the refinement of the α -Mg matrix and the redistributed precipitates. Douglas^[10] and Liu^[11] constructed large-sized Al alloy and Mg alloy sheets by multi-pass FSP, separately.

Nevertheless, there are still several problems with the FSP of Mg alloy. Previous studies^[8,12-14] have demonstrated that the HAZ temperature of magnesium alloys during FSP can be as high as 350 °C to 450 °C (recrystallization temperature ≈ 0.4 to $0.7 T_m$), which can lead to larger grain size in the SZ and HAZ and no twinning, although the maximum temperature of Mg alloy is lower than its melting temperature. This phenomenon was reported by Lee *et al.*,^[15] who found that the grain size in the SZ can be larger than that of the base material. They attribute the cause to grain growth at high temperatures after welding. Indeed, the formation of twins will be beneficial to improve the synergistic effect of strength plasticity in magnesium alloys.^[16-19] Our team's previous research^[20] on dual-phase steel has shown that the inhomogeneity of microstructure along the thickness of SZ strongly will affect the mechanical properties and corrosion resistance.

Furthermore, the ductility of SZ is easy to reduce after FSP, which is always a major problem of FSP. Liu *et al.*^[21] estimated the mechanical properties of SZ in FSPed AZ31 and found that the elongation (El) of the SZ is significantly reduced compared to that of the BM. Zheng *et al.*^[22] performed multi-pass AFSP of AZ31. They discovered that the increase in the accumulated thermal cycles and inputs resulted in a relatively pronounced recovery. Similar results can be also found in the FSP of AE42.^[23] These results describe the fact that FSPed magnesium alloy still lacks a good balance between strength and plasticity. To improve the comprehensive performance of the FSPed Mg alloy, the HAZ should be reduced and the cooling rate of the workpiece should be increased. Therefore, lower heat input is required during FSP.

The research of Xu *et al.*^[24] proved that SFSP was a very effective method to provide high-quality joints in a variety of materials by reducing the thermal cycle due to the high specific heat capacity of water. Furthermore, Mabuwa^[25] utilized the SFSP to prepare dissimilar aluminum alloy joints and certified that the SFSPed area was more ductile compared to the regular FSP. Also, Rouzbehani^[26] carried out friction stir welding of

Al-7075 alloy under water. They discovered that the underwater environment increased the precipitates' volume fraction and reduced the average grain. Derazkola *et al.*^[27] implemented FSW on dissimilar Al/steel joints with water cooling. They found that the maximum temperature decreased significantly and the formation of IMCs was limited due to low heat input.

It is well known^[28] that the ultrafine grain can allow for excellent strength–ductility synergy of the material. Hence, it is crucial to reduce the heat input in the FSP process, because the grains are difficult to grow under relatively low thermal cycling.^[20] It has been proven^[29] that configuring an additional cooling system to assist the FSP is an effective strategy for the preparation of ultrafine grain. It is worth mentioning that Mg alloys with HCP structure not only have low stacking fault energy^[30] but also are prone to twinning in the process of the SPD.^[31] The appearance of twins is beneficial to alleviate dislocation packing at GBs, thereby increasing the ability of grains to store dislocations to enhance plasticity.^[22] Not long ago, Tan *et al.*^[32] implemented FSP on AA 3003 aluminum alloy sheets under different cooling conditions and found that the size of recrystallized grains in SZ decreased obviously with decreasing welding ambient temperature.

As mentioned earlier, SFSP can significantly dominate the heat input of SZ. Furthermore, SFSP exhibits potential advantages in preparing Mg alloys with ultrafine grains and twinned structures. The lower melting point and susceptibility to oxidation cause Mg alloys to be extremely sensitive to temperature and processing atmosphere. As a consequence, SFSP may be a more ideal processing way for Mg alloys. However, so far, there are few relevant investigations on the SFSP of magnesium alloys. Although there have been some implementations of SFSP for Mg alloy,^[8,30,33,34] the cooling device they use cannot achieve water circulation, so the cooling effect is restricted. At the same time, these studies lack a comprehensive discussion on mechanical properties.

In this study, the SFSP on Mg–Al–Zn alloy was implemented using a homemade cooling apparatus with circularly flowable normothermic water as a cooling medium. Meanwhile, AFSP was implemented to facilitate better analysis of the advantages of SFSP and thus probe the applicability of SFSP Mg alloy. The grain structure, twinning morphology, texture characteristics of SZ, and their effects on mechanical properties were explored systematically.

II. MATERIALS AND METHODS

A. FSP Experiment and Materials

The base materials (BMs) are the hot-rolled Mg–Al–Zn alloy plates with dimensions of 160 mm \times 120 mm \times 6 mm and their chemical composition includes 2.328Al, 0.993Zn, 0.351Mn, 0.054Si, 0.013Cu, and 96.261 Mg (wt pct). Four-pass FSP experiments were performed, respectively, while maintaining the same rotational (800 rpm) and transversal speeds

(50 mm/min). The rotation tool made of H13 steel, which underwent heat treatment, remained a tilt angle of 1.8 deg and an axial shoulder tie in the depth of 0.2 mm during processing at each pass. The tool with a shoulder diameter of 24 mm comes with a conical pin 5 mm in length, which has a root diameter of 6 mm and a base diameter of 4 mm. A newly high-efficiency cooling system was designed to obtain fast heat dissipation during the experiment, as shown in Figure 1(a). To transfer the heat generated between the tool and the sample during the FSP as quickly as possible, copper mold was used as a backing plate. On the one hand, a water tank is arranged on the upper surface of the copper mold, which can ensure the flow of cooling water. Room temperature water guaranteed to flow during the experiment always flooded the workpiece surface. The valves in the water inlet and water outlet can regulate the flow rate of water. On the other hand, two channels are machined under the surface of the copper mold through which cooling water can dip and flow. A water delivery device is used to ensure that the flow of water fills the channel. Both methods of water circulation are used simultaneously.

In order to verify the cooling effect of different coolants on the thermal cycle during FSP, a wireless temperature measurement system (WTMS) was used to measure the SZ and HAZ temperatures in real-time. Three K-type thermocouples with a diameter of 1 mm were inserted obliquely into the shoulder through-hole close to the SZ surface and in the advance side (AS) and retreating side (RS) HAZ of the sheet (Figure 1(a)). The feasibility of the WTMS has been verified by our team in previous studies, as described by Cao *et al.*^[20,35,36]

B. Microstructure Characterization

The samples perpendicular to the processing direction were prepared in order to analyze the microstructure of processed zones, as revealed in Figure 1(b). All samples used for analysis in this work were extracted from FSP

material by wire EDM (Electrical Discharge Machining). The normal, transverse, and processing directions were denoted as ND, TD, and PD, severally. The optical microscopy (OM: OLYMPUS GX51), electron backscattered diffraction (EBSD: Zeiss sigma 300), transmission electron microscope (TEM: JEOL JEM-2100 Plus), X-ray diffraction (XRD: Malvern Panalytical, Empyrean) were used. The samples for OM were ground, polished, and etched for 5 seconds in a mixed liquid consisting of 1.5 mL HNO₃ + 1 mL CH₃COOH + 1 g H₂C₂O₄ + 150 mL H₂O. The samples for EBSD were mechanically ground, mechanically polished, and electropolished in 10 pct HClO₄ + 90 pct ethanol at -30 °C and 20 V. After a lot of attempts, it was determined that the scanning area is 400 × 300 μm with a step size of 0.4 μm. The scanning area for all EBSD tests was kept the same size and the same step size. The same data cleaning was performed using Channel 5 and AZtecCrystal software so that the data could be compared. An equivalent circle diameter is used to evaluate grain size. The average grain size (AGS) is the average value of the equivalent circle diameter of all grains. The calculation formula is $d_{AGS} = D/N$, where D is the sum of the sizes of all grains being counted; N is the total number of grains to be counted. The grains counted must be complete grains and exclude grains at the boundary of the scanning area and grains smaller than 0.8 μm (two steps). In addition, low-angle GBs (LAGBs) are defined as the GBs with a misorientation angle between 2 and 15 deg, and high-angle GBs (HAGBs) refer to the GBs with a misorientation angle above 15 deg.

C. Mechanical Property

Microhardness distribution generally reflects the distribution characteristics of the microstructure and precipitate phases. The microhardness of the cross section of the samples after mechanical polishing was measured using a microhardness tester (MHV-1000). The test was

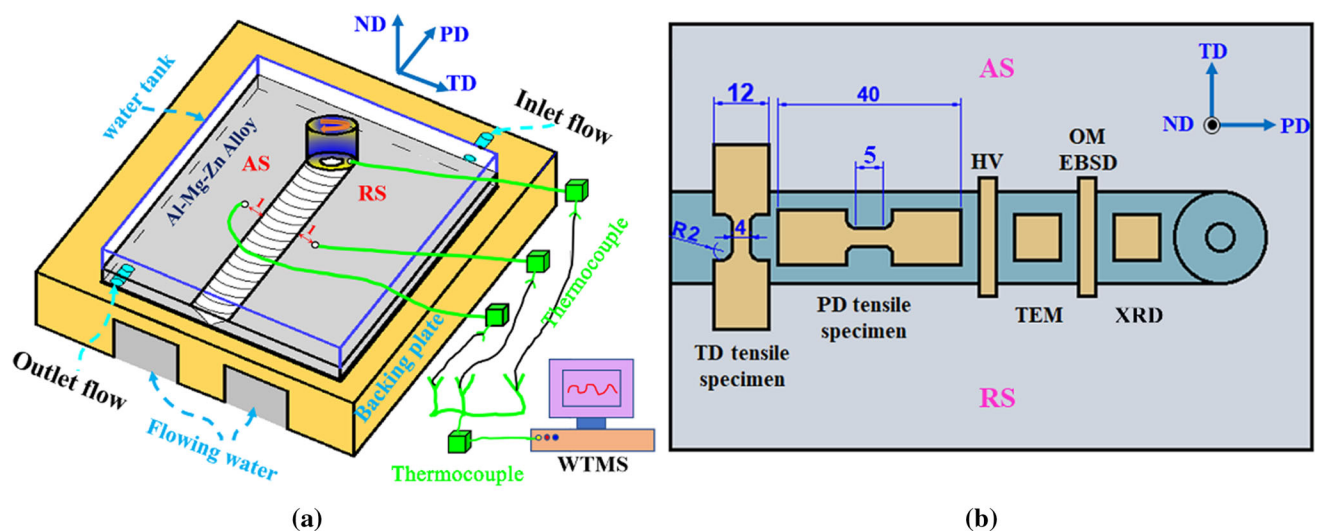


Fig. 1—(a) schematics of SFSP and WTMS; (b) illustrates the position and size of the measured specimen. (Unit: mm).

performed with a constant load of 0.98N, a holding time of 15 seconds, and adjacent test point intervals of 0.25 mm. The Origin software was used to draw the hardness cloud map to observe the change of microhardness more intuitively. Room temperature tensile tests were performed using an INSTRON 5965 testing machine with a strain rate of $8 \times 10^{-3} \text{ s}^{-1}$. Meanwhile, three tensile specimens with 3 mm thickness were made along the PD and TD for each sample to guarantee accuracy. Fracture topography and fracture characteristics were analyzed by using scanning electron microscopy (SEM, Hitachi S-4800). Figure 1(b) illustrates the shape and size of the tensile specimen.

III. RESULTS AND DISCUSSION

A. Thermal Cycling During Processing

The thermal cycle of the processed material plays a vital role in its structure and properties. It can give information on the maximum temperature reached by the material and the residence time of the material at a certain temperature, so as to determine the rate change of heating and cooling of the material in the processing process. Since the temperature history of each pass is similar, we take the temperature data of the fourth pass for representative analysis, as presented in Figure 2. The temperature history profile of the rotation tool is shown in Figure 2(a). The maximum temperature of SFSP was 291.7 °C, considerably lower than that of AFSP (421.1 °C). According to the Mg–Al phase diagram,^[37] eutectic structures that reduce the mechanical properties of materials will not appear during processing. According to Darras *et al.*,^[34] the thermal conductivity of materials has a great impact on the thermal field of the processed materials. High thermal conductivity will cause the temperature of the SZ to rise along the pass, and low thermal conductivity will easily lead to a higher temperature gradient. Compared with other engineering

materials such as aluminum alloys, the thermal conductivity of magnesium alloys is considered to be medium. Therefore, under the induction of flowing water, the temperature field of magnesium alloy is expected to become very stable. The thermal cycle curve shows that the temperature of SZ increases continuously during processing, but tends to be flat under immersion conditions. It implies that SFSP has a more stable thermal cycle for magnesium alloy than AFSP, which will be conducive to inducing the uniformity of structure and mechanical properties.

The temperature history of HAZ under air and water cooling is shown in Figure 2(b). The maximum temperature of AS is higher than that of RS, which has been reported in most of the literature.^[8,12,35,38] The maximum temperature of HAZ (AS-116.7 °C, RS-117.9 °C) in the water-cooled environment is noticeably lower than that in the air-cooled environment, and the temperature gap between AS and RS is significantly reduced. Temperature history implied that flowing water has a strong cooling effect during FSP, consistent with a previous report by Mabuwa *et al.*,^[25] the main reason for this is that the high specific heat capacity enables flowing water to acquire strong endothermic and heat dissipation capacities. It is easy to deduce that this precipitous cooling effect brought about by water cooling would inhibit heat conduction and thus influence the microstructure of the processing zone, especially reducing the grain size and the range of HAZ.

B. Macro-morphology and Microstructural Features

Figures 3(a) and (b) show the surface morphology after FSP in air- and water-cooled environments, respectively. In both cases, the surface morphology is excellent. In contrast, the surface color of SFSP is lighter, and the semicircular texture is more obvious due to the faster cooling speed. We also have similar results in the report of Chai *et al.*^[39] The reason can be relevant to the processing environment. SZ in direct contact with

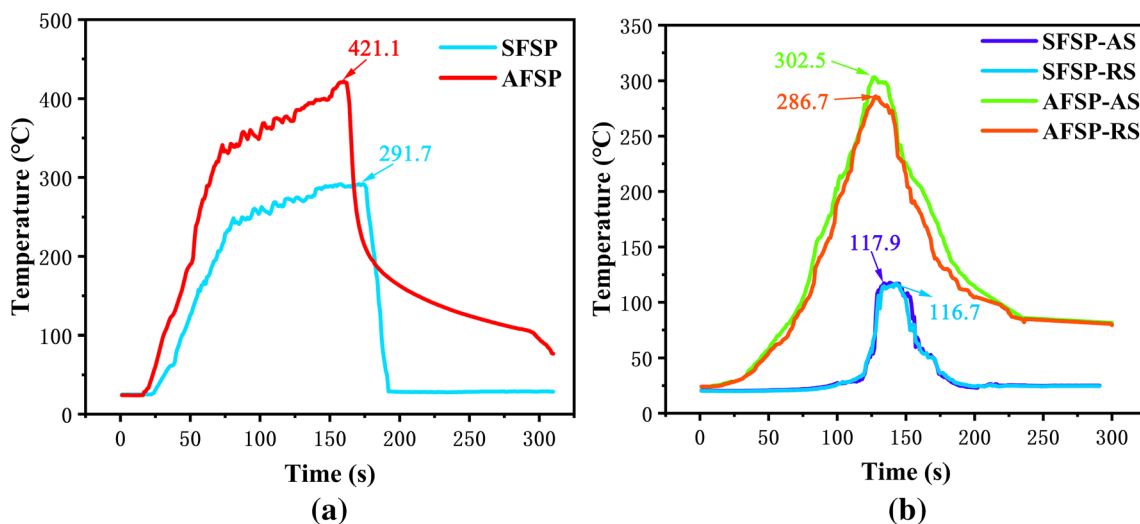


Fig. 2—Temperature history curves under different cooling environments. (a) The temperature history of rotating tools; (b) The temperature history of AS and RS.

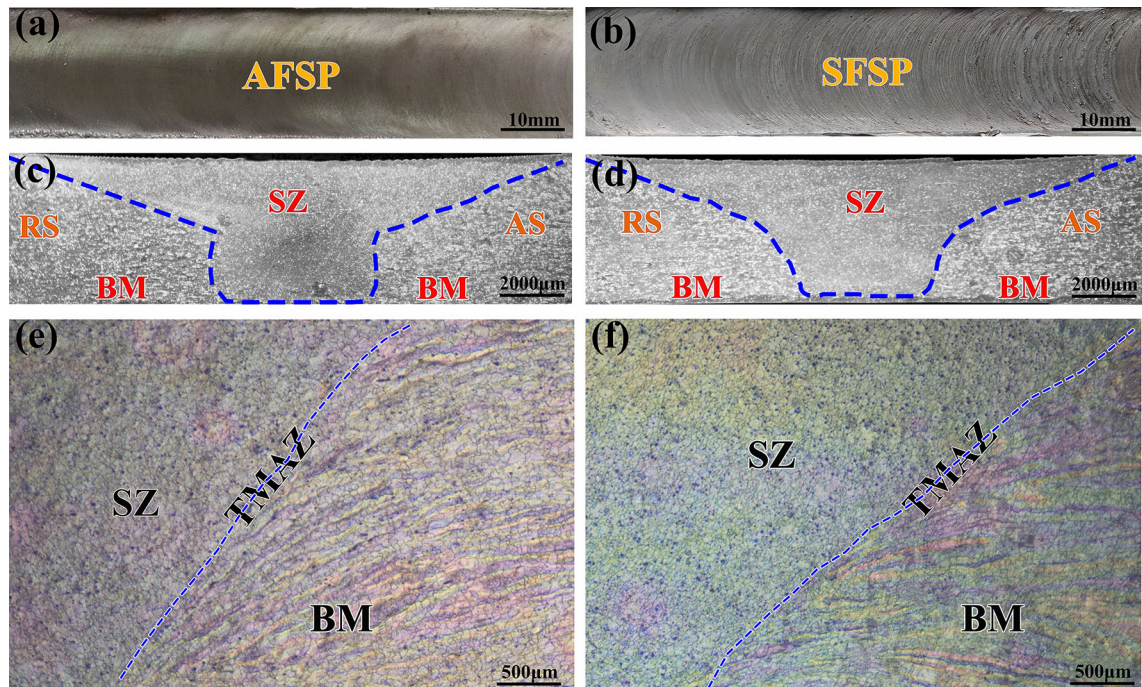


Fig. 3—(a), (c) and (b), (d) are the surface and cross-section views after AFSP and SFSP, respectively. (e), (f) are magnified views of AFSP and SFSP cross sections.

air will undergo severe oxidation at higher temperatures. Workpieces in a water-cooled environment are isolated from the air, so the surface is less likely to oxidize. Moreover, plasticizing Mg alloy would harden rapidly at fast cooling rates, which resulted in a more pronounced semicircular texture. Figures 3(c) and (d) show the cross-sectional morphology of AFSP and SFSP, respectively. Figures 3(e) and (f) are the enlarged views near the corresponding thermo-mechanical affected zone (TMAZ). No macroscopic defects such as tunnels and pores were observed in these cross sections. It is easy to recognize the three typical areas in the cross section including BM, TMAZ, and SZ. This is similar to the regional distribution analysis of Shahnami *et al.*^[30] The lower temperature of FSP compared to the melt welding process made it difficult to distinguish the heat-affected zone (HAZ) from the grain size. Therefore, we may as well group HAZ with TMAZ here. However, combined with the results of Ghetya *et al.*,^[40] it can be inferred that TMAZ would inevitably widen after four passes of AFSP due to excessive thermal effects and intense shear deformation.

The initial structure is a vital factor in determining the properties of metals and alloys. The EBSD analysis along the TD–ND plane is illustrated in Figure 4(a). It can be seen from the figure that the initial structure after hot rolling was not homogeneous. The grains were equiaxed but varied in size, and the AGS is about 10.2 μm , as shown in Figures 2(a) and (b). The grain boundary misorientation distribution confirms that there are very few twins and the twins with analogous orientations are shown by the black arrows in Figure 1(a). The HAGBs are as high as 69.85 pct (Figure 1(c)), which demonstrates that BM underwent a

long period of dynamic recrystallization (DRX) during hot rolling.^[41] About 3.31 pct of the GBs have a misorientation angle in the range of 86 ± 1.5 deg, which corresponds to the tension twin boundaries (TBs) misorientation in Mg magnesium alloys (86 deg).^[42] Moreover, the existence of twins is also stated by a distinct pole diagram analysis of the framed grain in Figure 4(a), as shown in Figure 4(d).

Figure 4(e) is the pole figure of BM. It can be seen from the figure that there is a pronounced basal texture in BM (texture strength as high as 19.29). Indeed, tensile twins are unfavorable to the activation of the basal slip system,^[43] which represents that the twins will be conducive to enhancing the mechanical properties of magnesium alloys. Previous studies^[44] have shown that basal slip and dynamic recovery of dislocations are the primary mechanisms of sharp texturing in magnesium alloys.

Figure 5 illustrates the EBSD results. In contrast to BM, grain refinement was obtained in both processing environments, especially under immersion conditions, as shown in Figures 5(a) and (b). The AGS of the AFSP region is about 6.5 μm (Figure 5(a)), while the AGS of the SFSP region was about 3.2 μm (Figure 5(b)). This can be explained by the difference in the temperature field. As mentioned in Section III–A, the thermal field was very responsive to the submergence conditions, which not only impacted the maximum temperature but also the time taken for the material to exceed a certain temperature. Lower maximum temperature and shorter high-temperature residence time led to more grain refinement and thus smaller grain size. Many previous research results^[20,25,45] can support this explanation. Furthermore, a large quantity of small-sized (less than

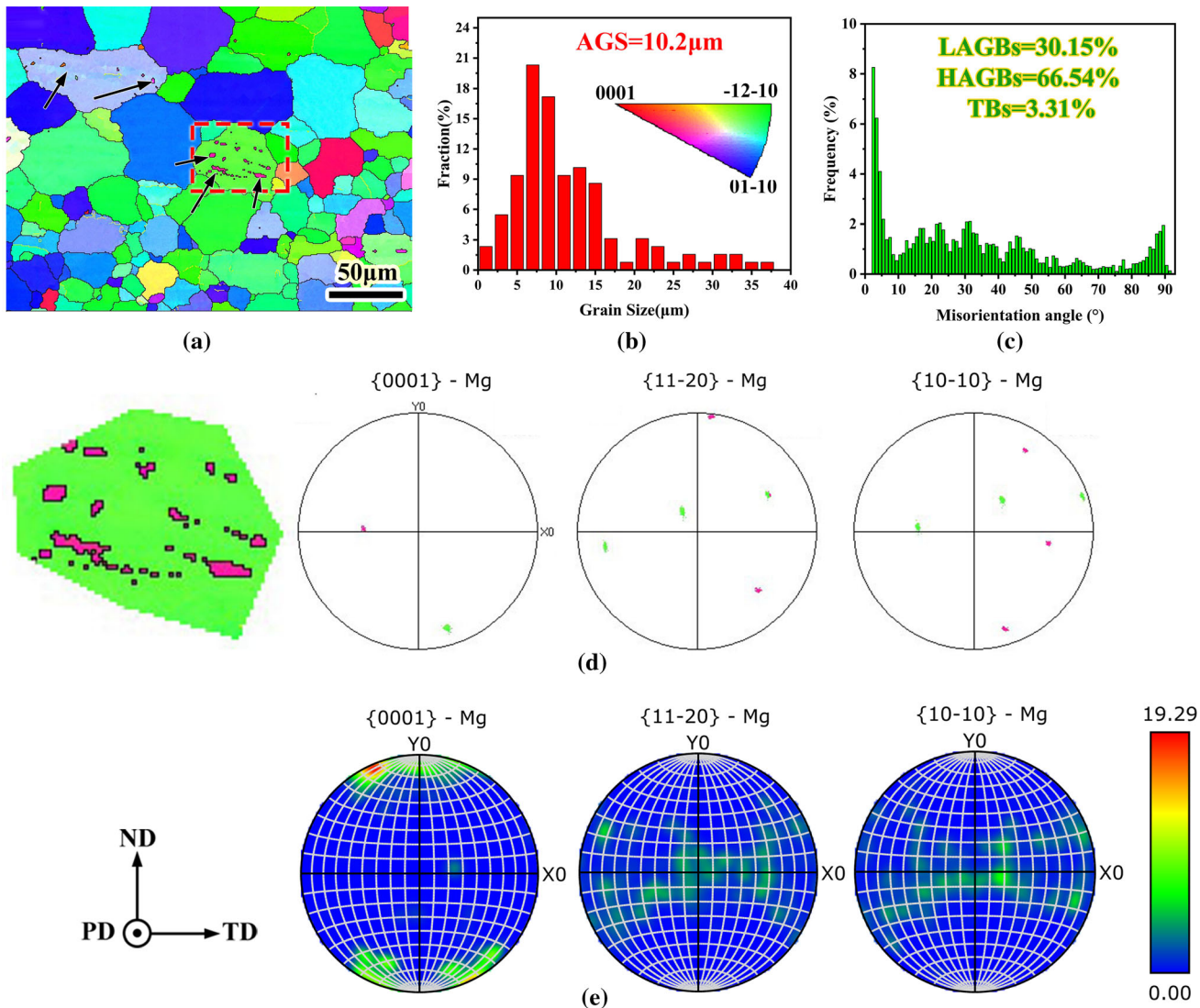


Fig. 4—Microstructure of rolled BM (a) IPF map of TD–ND plane; (b) grain size histogram in IPF map; (c) Grain boundary misorientation angle distribution of IPF map; (d) Grain and its pole figure corresponding to the red framed area in IPF map; (e) Pole figure analysis (Color figure online).

1 μm) grains with uniform orientation were observed in the SFSP region (Figure 5(b)). They can be judged as twin structures preliminarily by the analysis results of the BM. The formation of ultrafine twins effectively reduces AGS. Furtherly, there are three common twin structures in magnesium alloys, including the $\{1012\}$ tension twin, $\{1011\}$ compression twin, and $\{1011\}$ - $\{1012\}$ double twin, as verified by Liu *et al.*^[46]

Figures 5(c) and (d) illustrate that a higher proportion of twins are formed in the region after FSP compared with the BM. The principal twins are the tension twin and compression twin. The SFSP region forms a lot of tension twins, indicated by red (striped) and black (granular) arrows specifically in Figure 5(d). From Figures 5(e) and (f), the proportion of LAGBs increased after the FSP. However, the number of LAGBs below 5 deg in the AFSP region was significantly reduced, which was the result of a more sufficient DRX. Interestingly, both samples had a maximum of 86 ± 1.5 deg, indicating the presence of tension twins. It can be seen

quantitatively that the percentage of tension twin is up to 20.54 pct after SFSP, more than three times the AFSP area (5.51 pct). This phenomenon suggests that SFSP is an effective means of twinning magnesium alloys. As reported, the tensile twins are not conducive to dislocation slip,^[43] which means that the formation of tension twins is conducive to upgrading the mechanical properties of the processing zone. For the above results, we will make the following summary.

As a material with an HCP structure, the Schmid factor of the base plane and prismatic plane of magnesium alloy is small, which will make it difficult to start the slip mode so that twinning became the major plastic deformation mechanism. Therefore, the materials will flow tangentially under the driving of the high-speed rotation of the tool. When the shear stress in the twin direction reached the critical resolved shear stress, twins were generated. Shang *et al.*^[47] reduced the heat input by adjusting the process parameters and successfully introduced abundant twins in SZ. He also reported that the

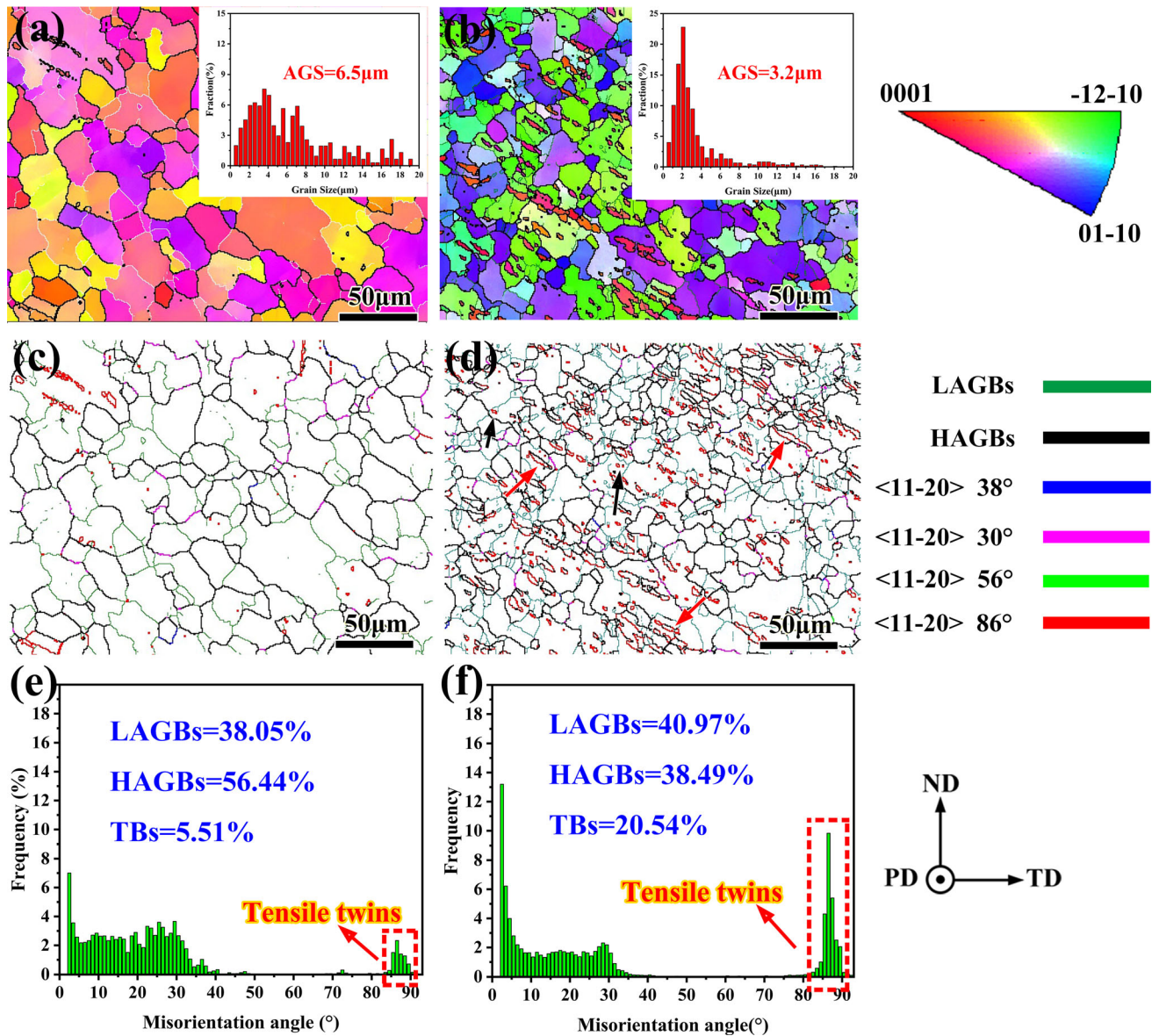


Fig. 5—IPF map, GBs, and Misorientation angle distribution under various cooling conditions: (a), (c), (e) AFSP; (b), (d), (f) SFSP.

increase in the extrusion force of the shoulder is conducive to the formation of twins. More specifically, the increased temperature led to a decrease in the axial force of the rotating tool, as demonstrated by Jain *et al.*^[48] The existence of cooling water can effectively reduce the heat input of the processing zone. Although the region of AFSP is also prone to form twins, due to the high heat input, the DRX is fully carried out, so fewer twins are left.

Additionally, the kernel average misorientation (KAM) value in the SFSP region is 0.65 deg, higher than that in the AFSP (0.42) and BM (0.55) region, as shown in Figures 6(a) through (c). KAM is commonly used to characterize the local strain distribution in metallic materials and KAM is positively correlated with dislocation density.^[49] Therefore, the dislocation density of different specimens can be compared by KAM with the same step size. Cao *et al.*^[20] recently

found that the average value of KAM was larger in the area with large dislocation density. This means that the dislocation density in the SFSP region has significantly increased compared to the AFSP region. It is worth mentioning that the KAM of AFSP was lower than that of the BM, which means that the SZ of AFSP underwent more DRX, which led to a decrease in dislocation density. The degree of recrystallization was additionally characterized using Grain Orientation Spread (GOS), which is consistent with KAM's discussion, as shown in Figures 6(d) through (f). The average GOS value (GOS_{AVE}) of the AFSPed sample is the smallest (1.21), which indicates that the AFSPed sample underwent the fullest recrystallization. The GOS_{AVE} of the SFSPed sample reached 2.56, which suggests that insufficient dynamic recrystallization occurred in the SZ in the rapid cooling environment, which leads to an increase in KAM values.

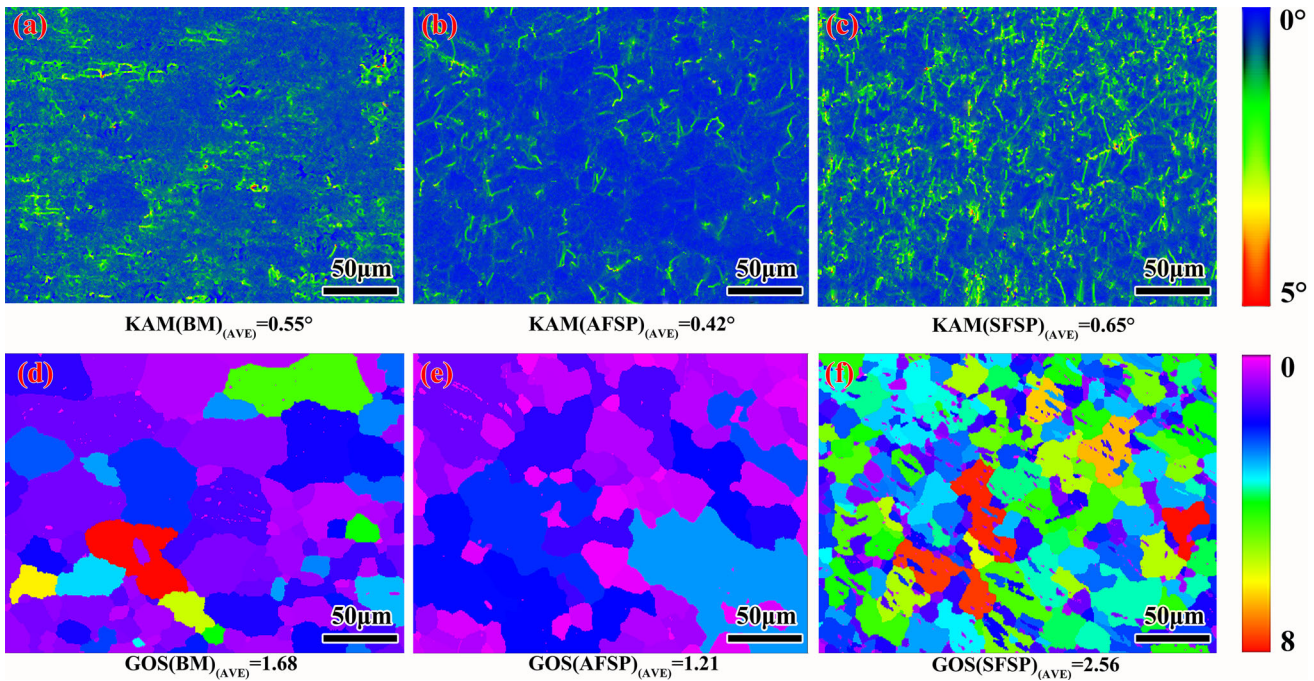


Fig. 6—(a) to (c) represent KAM maps of BM, AFSP, and SFSP, respectively. (d) to (f) represent GOS maps of BM, AFSP, and SFSP, respectively.

It is known from Figure 4(e) that the $\{0001\}$ orientation (texture) of the grains in the BM tended to be close to the south and north poles of the pole figure, and the distribution is relatively random. After FSP, the proportion of grains with $\{0001\}$ preferred orientation increased and tended to rotate toward the south pole of the projection plane, as shown in Figure 7. It illustrates that the vigorous stirring of the rotation tool will have a vital influence on the texture during the FSP. In fact, the material flow near SZ is complex and directly driven by the rotation of the mixing pin.^[50] The SFSP samples exhibited pronounced texture features with a c -axis almost 16 deg away from ND and almost 85 deg away from TD, as illustrated in Figure 7(a), from which the formation of a typical texture in the SZ can be deduced. The SZ of the AFSP also showed drastic textural features with the c -axis almost 49 deg away from ND and almost 56 deg away from TD (Figure 7(b)). The pole densities of the AFSP and SFSP samples are close, which is about 2.5 times that of the BM. It is shown that the movement of GBs and the rotation of grain occurred simultaneously in both processing environments. The mechanical stirring of the rotating tool remained strong despite the diminished thermal cycling underwater.

It is worth mentioning that the collection positions of the specimens under both conditions are the same for both conditions and the final pole density is approximate, but there is a large difference in grain orientation (color of the inverse pole figure in Figure 5). The above phenomenon can be explained by the difference in shear stance and the deformation characteristics of the magnesium alloy itself.^[51,52] Magnesium alloys usually form a strong shear texture under shear deformation conditions, but this shear texture is similar to rotating because

of the different strain fields. The deformation of materials is mainly shear during FSP, and the different shear stress fields will produce different grain orientations. During the FSP of magnesium alloys under different cooling environments, dynamic recrystallization is unable to eliminate the orientation generated by shear stresses in the SZ. Thus, even though we consider that EBSD data are obtained in similar areas, different grain orientations still exist because of different shear stress fields.

Figure 8 shows the XRD analysis results of the samples. The results show that both the base metal and the FSP specimens are principally composed of α -Mg. No other secondary phases were found, probably due to the low content. We believe that the main reason for the decrease in diffraction peak intensity after FSP is the change in grain size.

This can be explained by the Scherrer formula^[53]:

$$D_{hkl} = (k\lambda) / (\beta \cos\theta_{hkl})$$

among β is the half peak width; D_{hkl} is the grain size in the normal direction of $\{hkl\}$ crystal plane; k is the shape factor; θ is the angle of incidence; λ is the wavelength.

Therefore, when the X-ray incident on a small crystal, its diffraction line will become dispersive and broadened. The smaller the crystal grain, the wider the X-ray diffraction band or the lower the intensity. In addition, the crystal orientation is also an important factor. After FSP, the basal plane in SZ undergoes vigorous agitation and tilt, resulting in a low (0002) diffraction peak. The analysis in Figure 7 has already revealed that FSP caused the basal plane texture to deviate significantly from the TD direction, which led to a decrease in the intensity of the diffraction peaks.

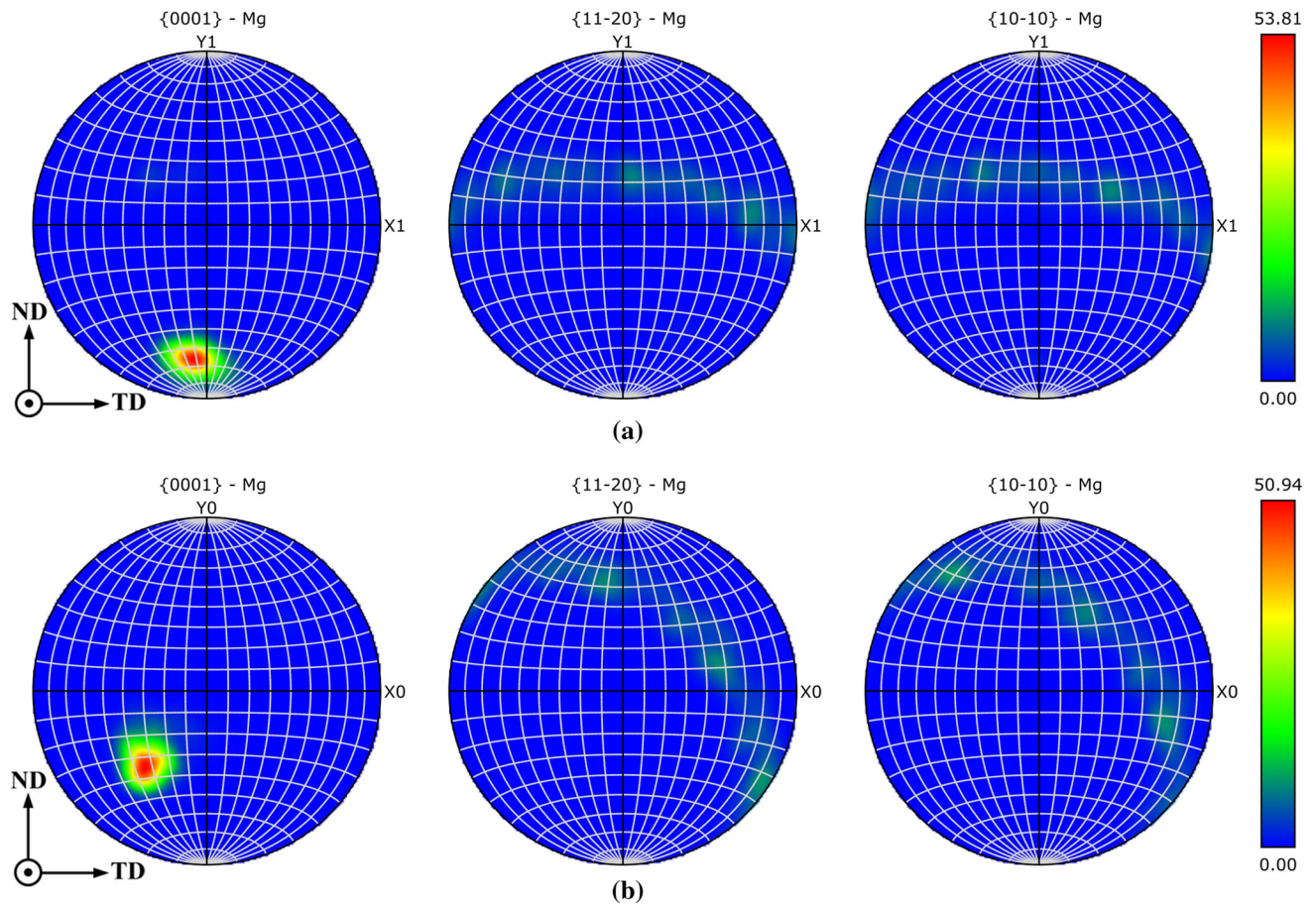


Fig. 7—Pole figures of specimens under water- and air-cooled environment: (a) SFSP; (b) AFSP.

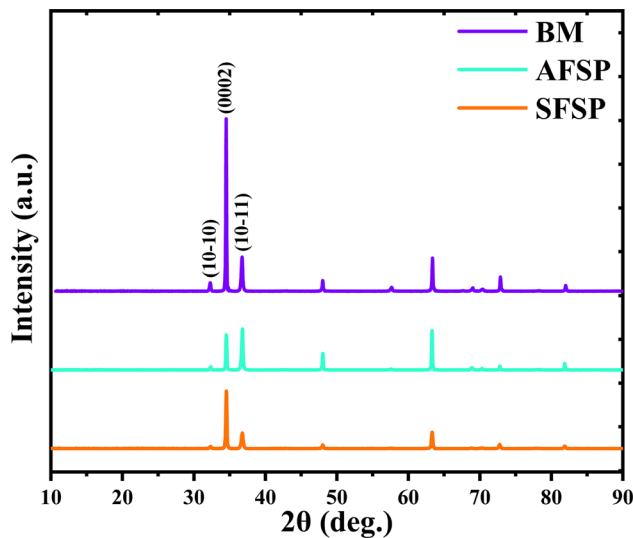


Fig. 8—XRD patterns of Mg-Al-Zn alloy in different states.

In order to analyze the microstructure of SZ more deeply, the distribution of dislocations, twins, and precipitates was observed by transmission electron microscope, as presented in Figure 9. After hot rolling, the grain size of the BM was coarse and there were a few dislocations in some grain boundaries, as presented in

Figure 9(a). Twins were not observed in BM because of the rare amount. The dislocation density increased evidently after four passes of FSP compared to BM, especially for SFSP samples. Many dislocation tangles and dislocation walls were induced in grains and deformed twins, as shown in Figures 9(b) and (c). This phenomenon quite corresponded well with the EBSD analysis, which completely illustrated that higher dislocation density and more ultrafine twins appeared in SFSP. The essential reason for the phenomenon was that the based slip system can be activated due to the low critical resolved shear stress, and high-density dislocations were formed in the twin region.^[54]

The SZ was exposed to severe thermoplastic deformation and dynamic recovery (DR) during FSP, and thus DRX occurred under the strong mechanical stirring of rotating tools. Subsequently, fine recovery grains and recrystallized grains formed. A lot of studies^[55–58] have verified that dislocations will decrease sharply during DRX. There are fewer dislocations other than twins in the SZ of AFSP, and some sub-GBs are found (Figures 9(b) and (e)), which signifies that the DR and DRX are fully carried out because multi-pass processing provided multiple thermal cycles. According to Liu *et al.*,^[7] the increase of heat input was conducive to stimulating the DRX of magnesium alloy, but it is also easy to lead to the growth of the second-phase particle.

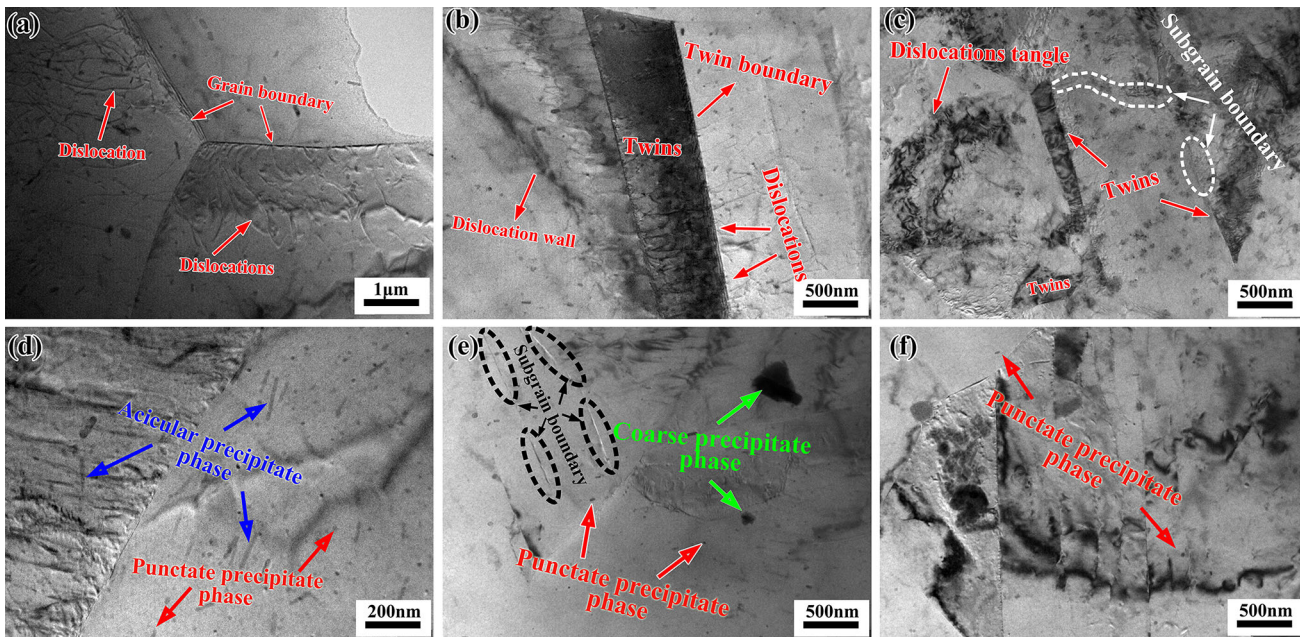


Fig. 9—The TEM images of different regions: (a) to (c) are the dislocation density in BM, AFSP, and SFSP regions, respectively; (d) to (f) are the precipitate distribution characteristics in BM, AFSP, and SFSP regions, respectively.

Meanwhile, a lot of dislocation tangles and sub-GBs can be found in the SZ of SFSP. According to Wang *et al.*,^[18] the TBs will continuously absorb the sub-GBs so that HAGBs would gradually form when magnesium alloy was subjected to high-speed strain. This process is called twin-induced DRX, which means that SZ underwent violent DR, but the DRX was not sufficient due to the lack of heat input and lots of dislocations were retained. Interaction between dislocations led to slip difficulties and then the formation of dislocation walls. The subsequent dislocation will be harder to move through it. Eventually, dislocation walls that have absorbed enough dislocations will transform into dislocation tangles. Some dislocation entanglements and dislocation walls were left and formed isolated segments inside the grains and at grain boundaries.

The difference in precipitation phase distribution was also noteworthy. The precipitated phase of BM was shown as a large amount of acicular-like (marked by the blue arrow) and punctate-like (marked by the red arrow), as shown in Figure 9(d). The precipitates were primarily distributed in dispersed punctation after FSP. Some coarse precipitates were formed in the AFSP region because of the higher processing temperature (Figure 9(e)), while the precipitates in the SFSP region were more dispersed and homogeneous (Figure 9(f)). It has been reported^[7] that the precipitates of AZ31 will undergo “dissolution-precipitation-growth” during FSP. Therefore, the final precipitate morphology and size in the SZ often exhibit significant differences from BM. They will inevitably dissolve into α -Mg under the thermal effect.^[59] A lot of metastable phases and supersaturated solid solutions were formed because the thermal cycling increased the diffusion rate of atoms and shortened the diffusion distance.^[23] In the subsequent

cooling stage, a lot of precipitates grew (Figure 9(e)) due to the high-temperature residence time in the AFSP region, while the fine-dispersed precipitated phases in the SFSP region were retained under the condition of rapid cooling. According to the Orowan mechanism,^[11] small dispersed precipitates contribute very significantly to the increase in strength. The above results indicate that the precipitation morphology of SFSP samples is consistent with our expected results.

C. Mechanical Properties

The cloud maps of both samples in Figure 10 revealed the microhardness characteristics. The average hardness of the AFSP sample is 69.5HV, which is slightly higher than the average hardness value of BM (62.6HV). In contrast, the microhardness in SZ of the SFSP sample with 86.3HV has a relatively high hardness value. The samples produced a large-scale HAZ after four passes of AFSP, but the HAZ of SFSP samples was not evident in the hardness cloud map. This is because the water-cooling effect reduced the influence of the thermal cycle on HAZ so that HAZ retained the microhardness equivalent to that of the BM. The above phenomenon is consistent with the conjecture of Figure 3.

It has been reported that FSP/W will form softening or hardening zones. When the strengthening precipitates are coarsened and dissolved, it will lead to softening of SZ and HAZ, which is especially noticeable in aluminum alloys.^[26,45,58] Related reports also verified that the SFSP of aluminum alloy can weaken the softening effect caused by the precipitation phase through grain refinement.^[56] For magnesium alloys, most of the available reports show that the microhardness of SZ increases with the decrease in grain size.^[7,8,15,47,60–62] Our results are in perfect agreement with it.

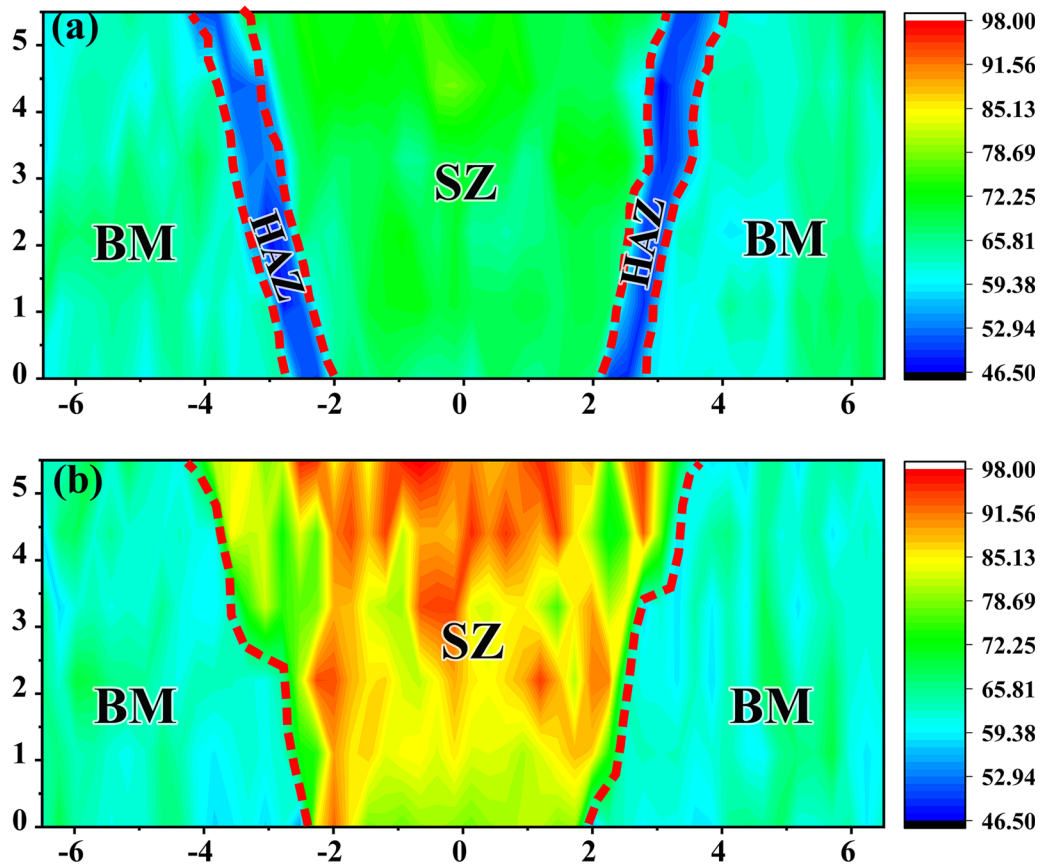


Fig. 10—Microhardness distribution cloud plots of cross section under different cooling environments: (a) AFSP; (b) SFSP.

In fact, the microhardness value is closely associated with the thermal history. Temperature distribution impacted the size and distribution of grains and precipitates. According to the well-known Hall–Petch relation,^[63] an increased grain refinement effect led to increased hardness. Nevertheless, the microhardness of the AFSP samples did not increase significantly after grain refinement. This can be explained by the change in dislocation density. A decrease in dislocation density led to a decrease in microhardness.^[26] Sufficient DRX led to a rapid drop in the dislocation density, even lower than that of the BM, as shown in Figure 6(c), which weakened the grain refinement strengthening effect. The ultimate result of this “strengthening-weakening” effect is a slight increase in microhardness. On the contrary, in addition to the more pronounced grain refinement of the SFSP sample, the insufficient twin-induced DRX led to the retention of a large number of dislocations in the SZ, which are key factors for the enhancement of the SZ microhardness of the SFSP. Equally crucial, the contribution of the twinning-induced hardening effect to the microhardness was also considerable. In explaining the hardening mechanism of titanium alloys, Fitzner *et al.*^[64] mentioned that the major contribution of twins to the hardening of titanium alloys was by reorientation-induced hardening through tensile twinning. This theory is also applicable to magnesium alloys because of the same HCP structure. Magnesium alloys with poor plastic deformation ability

are prone to form strong texture (Figure 7) in SZ during SFSP, LAGBs provided a restricted barrier effect on dislocation movement and twinning transmission, so the k values (Hall–Petch slope) of the FSPed magnesium alloys are relatively low^[47,65] compared to magnesium alloys constructed by other processing methods. Consequently, the contribution of grain refinement on microhardness was less pronounced than that of twinning-induced hardening. From this perspective, the twin-induced hardening effect and high dislocation density may be the dominant role for the increased microhardness of SZ.

Tensile properties of BM, TD-SZs, and PD-SZs manufactured in different processing environments are shown in Figure 11. For simplicity, the AFSP and SFSP samples along the transverse and processing directions are denoted as AFSP-TD, AFSP-TD, SFSP-TD, SFSP-TD, respectively. Figures 11(a) and (b) show the mechanical property of the AFSP-TD and SFSP-TD. The FSPed samples show higher ultimate tensile strength (UTS) than BM (275 MPa) and the SFSP sample exhibits higher UTS (349 MPa) than AFSP (296 MPa). The EI of the AFSP specimen increased to 27 pct compared to BM of 24 pct. The EI of the SFSP sample was reduced to 20 pct, but the yield strength (YS) (199 MPa) significantly increased compared to the BM (161 MPa), while the YS of AFSP decreased to 153 MPa. Although the EI of the AFSP-PD was further improved, it was still lower than the YS of the BM, as

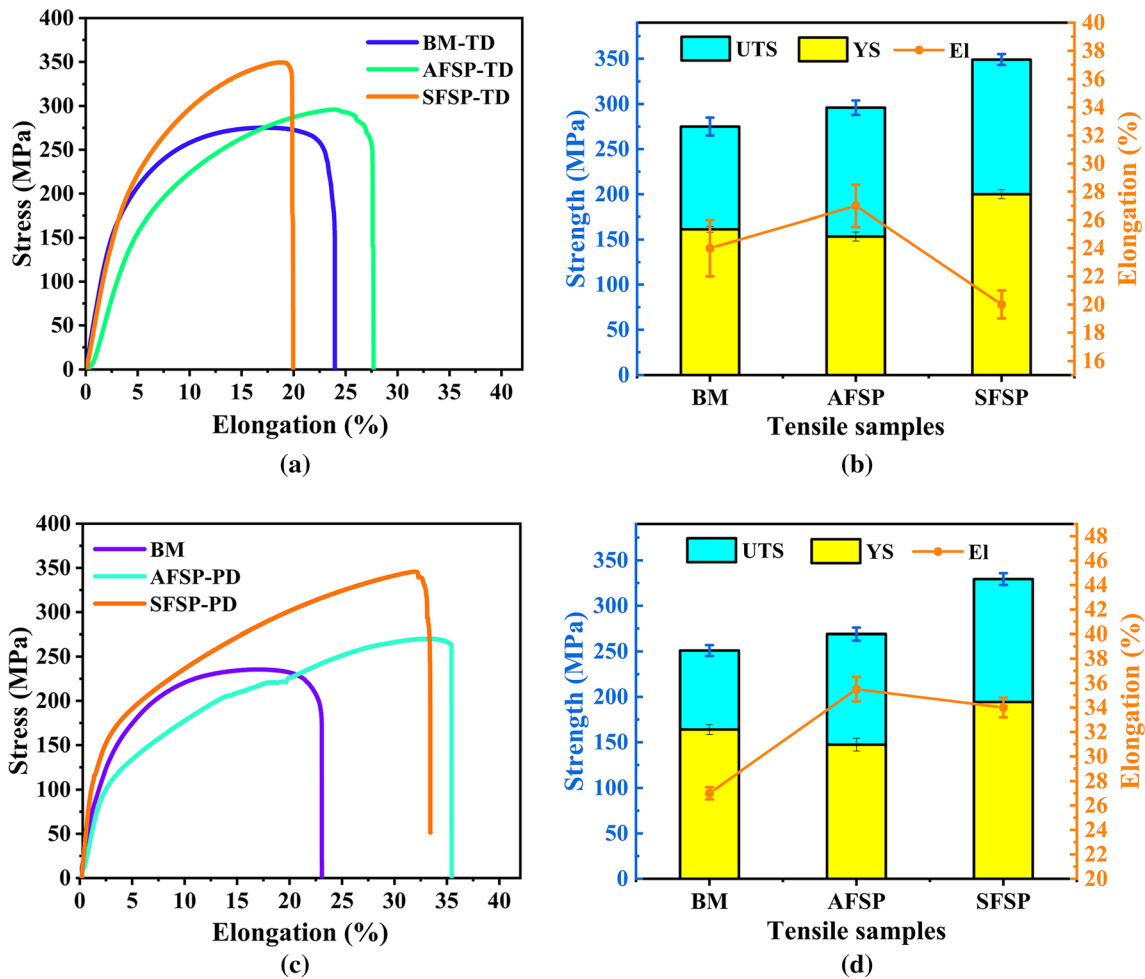


Fig. 11—Mechanical properties of BM, AFSP, and SFSP along the TD and PD directions, respectively. (a), (c): engineering stress-elongation curves; (b), (d): average UTS and EI statistics of the corresponding stretched samples.

shown in Figures 11(c) and (d). Surprisingly, the YS, UTS, and EI of the SFSP-PD have surpassed the BM. In summary, a satisfactory synergistic strength–ductility improvement was obtained for the SFSP-PD.

There are three questions here that need to be discussed in depth: (1) Why do all samples show better plasticity along the PD? (2) What is the reason for the decrease in yield strength of the AFSP samples? (3) What is the mechanism by which SFSP samples synergistically improve strength and ductility along the PD?

Firstly, it was reported that the texture of SZ along the TD is inhomogeneous for Mg–Al–Zn alloys that have undergone FSP.^[66] The texture of the edges of the SZ is often different from the middle of the SZ, which will lead to poor intergranular coordination and thus stress concentration, as shown in Figure 12(a), while stretched sample can be uniformly deformed in the PD direction (Figure 12(b)). As a result, the ductility of samples along TD is always poorer than that of PD specimens, regardless of whether they are AFSP or SFSP samples. In particular, the SFSP-TD samples lost 4 pct of plasticity due to the uneven texture and the high dislocation density. If the size of the tool pin is increased to expand the width of the SZ, excel

strength-productivity along the TD is promising. Secondly, as mentioned above, the SZ of AFSP got significantly finer and the dislocation density was lower than that of the BM, which implied that the ability of the grains to contain dislocations increased during room temperature stretching.^[20] This seems to counteract the unfavorable effect of the inhomogeneous texture along TD. Therefore, the AFSP samples exhibit good plasticity both along the TD and also the PD. However, this also leads to a decrease in yield strength. Therefore, it is difficult for AFSP to realize the synergistic improvement of the strength and plasticity of magnesium alloys.

Thirdly, the strengthening effects of the SFSP-SZ were mainly attributed to fine-grain strengthening, twins strengthening, and dislocation strengthening. Ultrafine grains and twinning can contribute to reinforcement^[32,67] and the retained large number of dislocations provided resistance to the movement of dislocations.^[20] The result was a significant increase of YS and UTS. Meanwhile, the plasticity of the SFSP-PD samples was significantly improved because the texture along the PD was even and refined grain can also improve plasticity. The appearance of twins is beneficial to alleviate dislocation packing at GBs, which can increase the

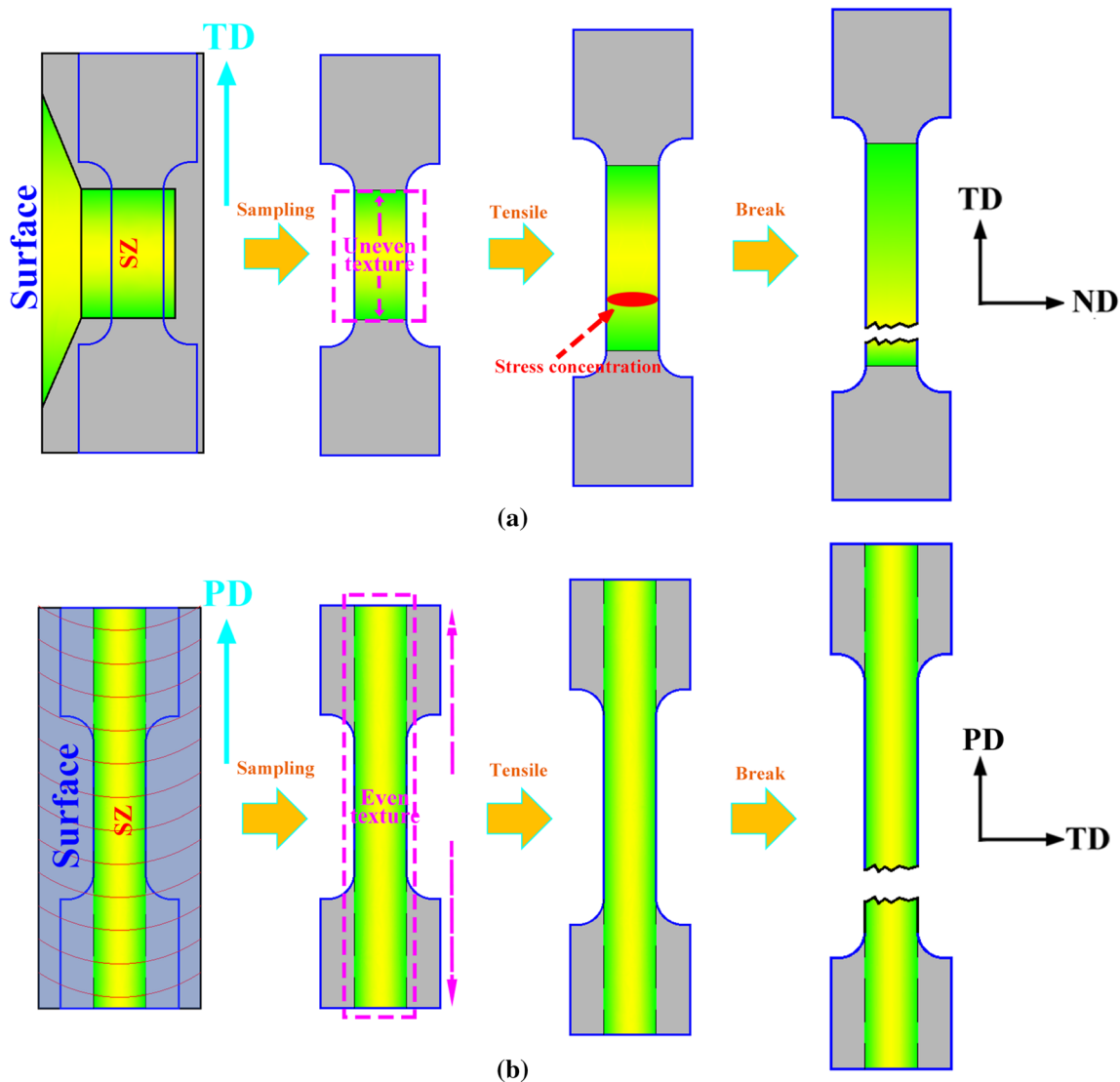


Fig. 12—Mechanism diagram of different ductility in different stretching directions: (a) TD; (b) PD.

ability of grains to store dislocations to enhance plasticity.^[22,67] In summary, fine-grain strengthening and twin strengthening are effective means to realize the synergistic strength–ductility improvement of magnesium alloys, which can overcome the unfavorable effect of high dislocation density on ductility. In addition, reducing the loss of plastic SFSP samples (containing a high density of dislocations) requires avoiding uneven texture.

This phenomenon can also be illustrated by the dislocation slip feature. The ability of dislocations to be activated was also critical for the plasticity of magnesium alloys. It is well known that the plastic deformation of magnesium alloys at room temperature was predominantly dominated by basal plane slips.^[23] Figure 13 illustrates the Schmidt factor (SF) distribution of the basis slip system ($\{0002\}\langle 11\bar{2}0 \rangle$) of SZ at room temperature.^[68] The SF diagrams come from the microstructure of the specimen in Figure 5. It can be seen that the Schmidt factors along the TD

(Figures 13(a) and (c)) were lower than that along the PD (Figures 13(b) and (d)), which means that the basal plane slip was more easily activated along the PD. Therefore, SZs have higher plasticity along PD, which agrees well with the results of mechanical properties. In addition, most of the twins were in a soft orientation (darker color), as shown in Figures 13(c) and (d). This means that twinning can increase the ability of grains to accommodate dislocations by absorbing dislocations during forming. The Schmidt factor reduction of the grains and the promotion of twinning together enhanced the EI when the forming appeared along the PD. Beyerlein *et al.* reported that deformation twinning frequently exhibits non-Schmid behavior.^[69] In addition to ambient temperature and Schmidt factor, grain size and grain boundary misorientation have a strong influence on twinning behavior.

The tensile fracture morphology was characterized as shown in Figure 14. It can be seen from Figure 14(a) that a step-like morphology emerged at the fracture of

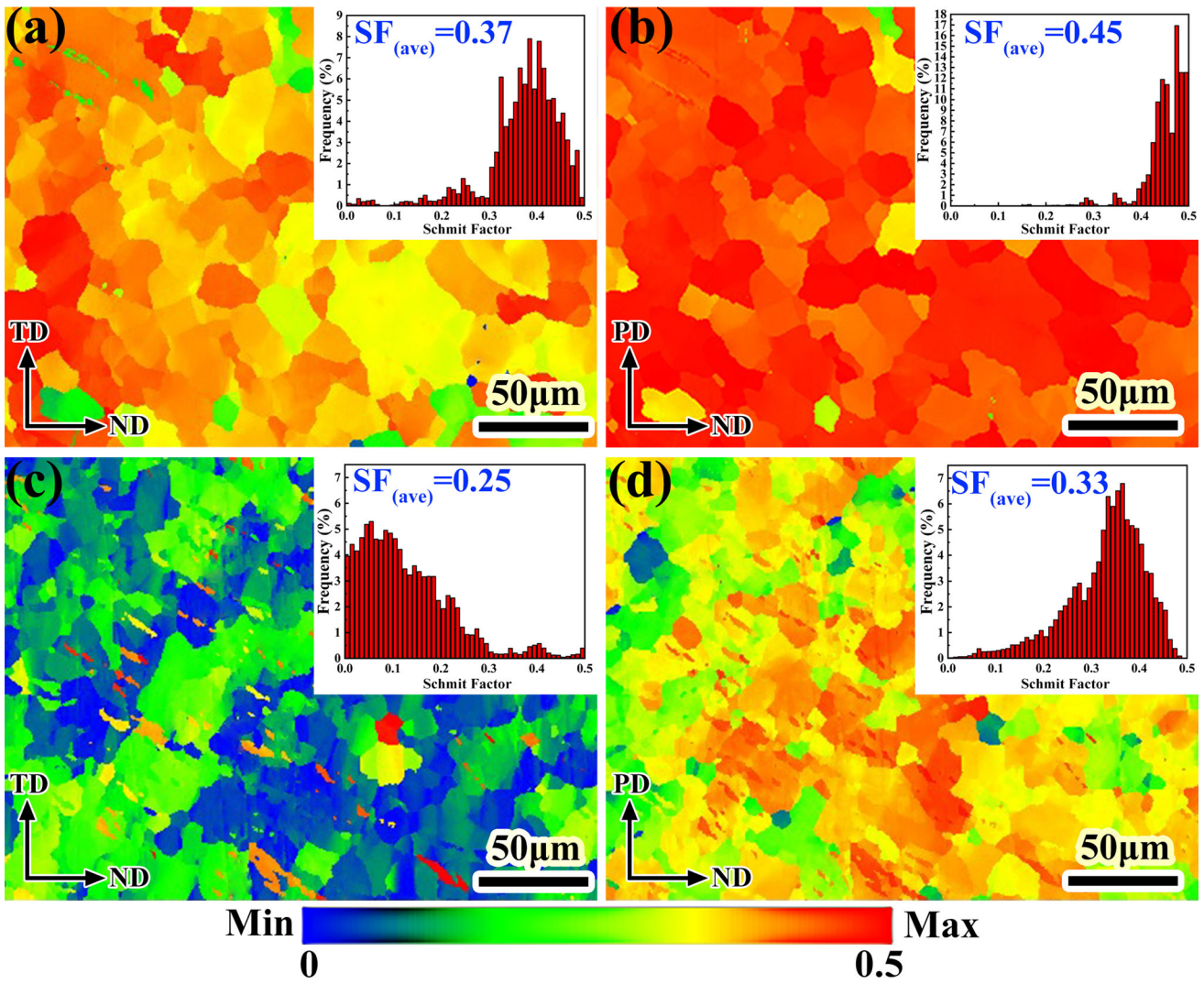


Fig. 13—The Schmid factor distribution of $\{0002\}\langle 1120 \rangle$ basal slip under different cooling environments: (a) AFSP-TD; (b) AFSP-PD; (c) SFSP-TD; (d) SFSP-PD.

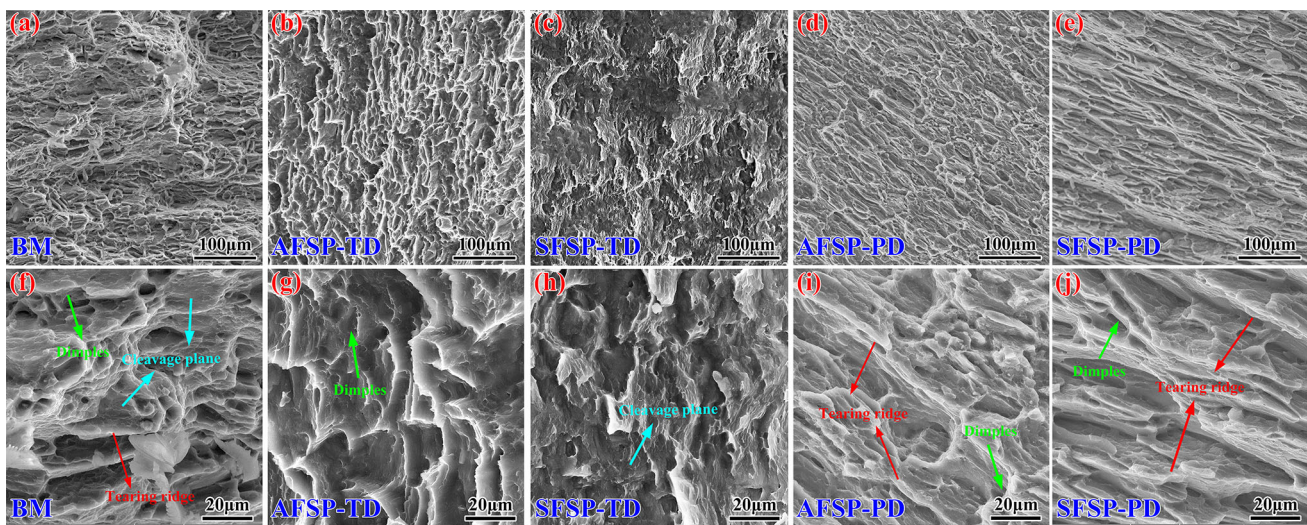


Fig. 14—SEM images of tensile fracture surfaces: (a, f) BM; (b, g) AFSP-TD; (c, h) SFSP-TD; (d, i) AFSP-PD; (e, j) SFSP-PD.

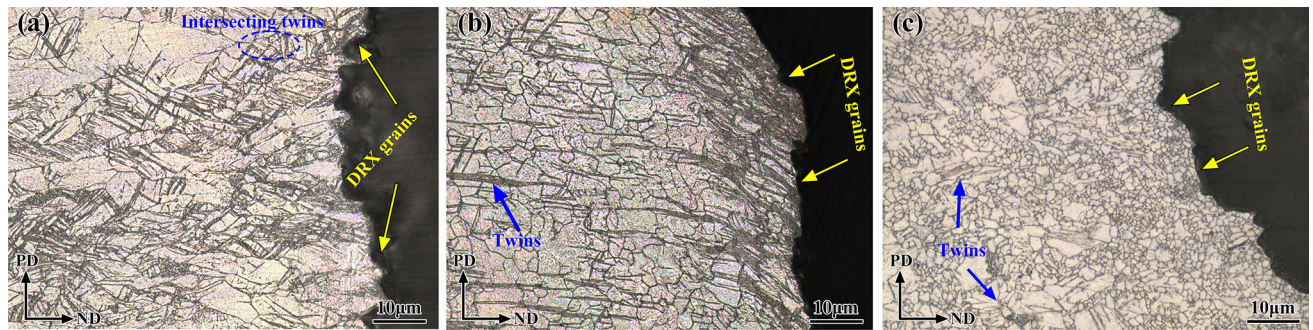


Fig. 15—OM images of tensile fracture surfaces: (a) BM; (b) AFSP-PD; (c) SFSP-PD.

the BM specimen, which was due to the presence of a heap of coarse precipitates in the BM. The regions rich in precipitates were prone to stress concentration during the deformation process, which not only provided nucleation sites for cracks but also changed the propagation path of cracks.^[23] Fine dimples, cleavage planes, and tear ridges appeared on the BM fracture at high magnification (Figure 14(f)), which indicates that the tensile fracture mode of the BM specimen is more inclined to brittle fracture. The fracture surface of AFAP-TD is characterized by large dimples (Figures 14(b) and (g)), which indicates better plasticity during stretching. However, the dimples on the fracture surface of SFSP-TD became blurred (Figures 15(c) and (h)), indicating a reduced level of plastic deformation.^[70] In contrast, the dimples of the AFSP-PD and SFSP-PD are more and deeper (Figures 14(b) and (c)). A large number of large tear ridges and small shear lips imply that the failure mode was a mixed ductile–brittle fracture mode dominated by ductile fracture. It shows that the FSP-PD samples showed good plasticity, which is consistent with the tensile test results.^[71] Particularly, the samples of SFSP exhibited larger and longer tear ridges (Figure 14(f)), which implied that significant strength and plasticity improvements were obtained simultaneously for the SFSP-PD specimen.^[39]

To further reveal the mechanism of SFSP-PD strength–ductility synergistic enhancement, the OM of the crack boundary along PD was analyzed as shown in Figure 15. Fine DRX grains and a large number of twins were observed on the BM crack boundaries. Initial coarse crystals were also observed, which indicated that the plastic deformation was inhomogeneous. In contrast, the plastic deformation of AFSP-PD is more uniform. More dense twins and DRX grains were observed at the crack edges. DRX grains in the vicinity of the crack have been reported to be caused by twins where sufficient strain may be present.^[72] Interestingly, dense twins were not observed at the fracture boundaries of the SFSP-PD samples, while equiaxed recrystallized grains dominated. A small number of elongated grains and intersecting twins are observed away from the fracture. This may be the result of fine grains and a large number of nano-twins with sufficient strain. As a result, the SFSP-PD samples are more prone to dynamic recrystallization during deformation to increase

intergranular coordination, which leads to a synergistic increase in the strength–ductility of SFSP-PD.

IV. CONCLUSION

High-quality modified regions with ultrafine grains and twins were successfully prepared by multi-pass submerged friction processing (SFSP) on Mg–Al–Zn alloys. The grain structure, twinning morphology, texture characteristics of the stirring zone, and their effects on mechanical properties were studied systematically. The following conclusions can be drawn:

1. SFSP with flowing water significantly reduced the maximum temperature compared to AFSP. Meanwhile, multi-pass SFSP was proved to be an effective means of twinning magnesium alloys.
2. SFSP inhibited recrystallization and grain growth compared to AFSP which had undergone sufficient recrystallization, which was conducive to higher dislocation densities.
3. Grain refinement, high-density dislocations, and twinning-induced hardening significantly increased the microhardness of the SFSP region.
4. It is difficult for AFSP to achieve a synergistic strength–ductility improvement in magnesium alloys because of the reduced yield strength, although grain refinement and reduced dislocation density were conducive to improved ductility. However, the ultrafine twinned magnesium alloys prepared by SFSP obtained a synergistic enhancement of the strong plasticity along the PD.
5. The SFSP-PD specimen failed in a ductile–brittle mixed fracture mode. Lots of tear ridges and numerous dimples demonstrate excellent mechanical properties.

ACKNOWLEDGMENTS

This work was supported by the National Natural Science Foundation of China (Grant No. 52275217). Tao Sun thanks the fund support given by the Nanjing University of Aeronautics and Astronautics “Post-graduate Innovation Experiment Competition”

Cultivation Project (No. 1006/016001). We thank the Technology Research Institute of Nanjing Chenguang Group Co Ltd for its great help.

CONFLICT OF INTEREST

The authors declare that they have no known competing financial interests or personal relationships that could have appeared to influence the work reported in this paper.

REFERENCES

1. T. Chen, W. Xue, Y. Li, X. Liu, and J. Du: *Mater. Chem. Phys.*, 2014, vol. 144, pp. 462–69.
2. W. Xu, N. Birbilis, G. Sha, Y. Wang, J.E. Daniels, Y. Xiao, and M. Ferry: *Nat. Mater.*, 2015, vol. 14, pp. 1229–35.
3. Y. Wan, B. Tang, Y. Gao, L. Tang, G. Sha, B. Zhang, N. Liang, C. Liu, S. Jiang, Z. Chen, X. Guo, and Y. Zhao: *Acta Mater.*, 2020, vol. 200, pp. 274–86.
4. I.H. Jung, M. Sanjari, J. Kim, and S. Yue: *Scr. Mater.*, 2015, vol. 102, pp. 1–6.
5. T. Homma, N. Kunito, and S. Kamado: *Scr. Mater.*, 2009, vol. 61, pp. 644–47.
6. G. Peng, Y. Hu, G. Dou, Y. Sun, Y. Huan, S.H. Kang, and Z. Piao: *J. Ind. Eng. Chem.*, 2022, vol. 110, pp. 414–23.
7. F. Liu, Y. Ji, Z. Sun, J. Liu, Y. Bai, and Z. Shen: *J. Alloys Compd.*, 2020, vol. 829, 154452.
8. W. Liu, Y. Yan, R. Ni, T. Sun, S. Wu, and Y. Shen: *Sci. Technol. Weld. Join.*, 2021, vol. 26, pp. 136–43.
9. Q. Liu, G. Chen, S. Zeng, S. Zhang, F. Long, and Q. Shi: *J. Alloys Compd.*, 2021, vol. 851, 156835.
10. D.C. Hofmann and K.S. Vecchio: *Mater. Sci. Eng. A*, 2005, vol. 402, pp. 234–41.
11. F. Liu, Y. Li, Z. Sun, and Y. Ji: *J. Mater. Res. Technol.*, 2021, vol. 11, pp. 1019–30.
12. H.T. Serindag and B.G. Kiral: *Lat. Am. J. Solids Struct.*, 2017, vol. 14, pp. 113–30.
13. S. Mironov, Y.S. Sato, and H. Kokawa: *Metall. Mater. Trans. A*, 2019, vol. 50A, pp. 2798–2806.
14. S. Mironov, T. Onuma, Y.S. Sato, and H. Kokawa: *Acta Mater.*, 2015, vol. 100, pp. 301–12.
15. W.B. Lee, Y.M. Yeon, and S.B. Jung: *Mater. Sci. Technol.*, 2003, vol. 19, pp. 785–90.
16. B.J. Lv, S. Wang, N. Cui, and F. Guo: *Mater. Sci. Eng. A*, 2021, vol. 809, 140986.
17. H.Y. Song, G.M. Evans, and S.S. Babu: *Sci. Technol. Weld. Join.*, 2014, vol. 19, pp. 376–84.
18. Z. Wang, G. Cao, F. Wang, L. Zhou, P. Mao, X. Jiang, and Z. Liu: *Mater. Character.*, 2021, vol. 172, 110839.
19. A. Malik, Y. Wang, C. Huanwu, F. Nazeer, B. Ahmed, M.A. Khan, and W. Mingjun: *Mater. Sci. Eng. A*, 2020, vol. 771, 138649.
20. F. Cao, G. Huang, W. Hou, R. Ni, T. Sun, J. Hu, Y. Shen, and A.P. Gerlich: *J. Mater. Process. Technol.*, 2022, vol. 307, 117660.
21. F. Liu, Y. Ji, and Y. Bai: *Trans. Nonferr. Met. Soc. China*, 2020, vol. 30, pp. 3263–73.
22. F.Y. Zheng, Y.J. Wu, L.M. Peng, X.W. Li, P.H. Fu, and W.J. Ding: *J. Magn. Alloy.*, 2013, vol. 1, pp. 122–27.
23. Y. Jin, K. Wang, W. Wang, P. Peng, S. Zhou, L. Huang, T. Yang, K. Qiao, B. Zhang, J. Cai, and H. Yu: *Mater. Character.*, 2019, vol. 150, pp. 52–61.
24. N. Xu, B. Gu, Y. Fan, J. Shen, Q. Song, J. Zhao, and N. Xu: *Mater. Sci. Technol.*, 2022, <https://doi.org/10.1080/02670836.2022.2105501>.
25. S. Mabuwa and V. Msomi: *J. Mater. Res. Technol.*, 2020, vol. 9, pp. 9632–44.
26. R. Rouzbehani, A.H. Kokabi, H. Sabet, M. Paidar, and O.O. Ojo: *J. Mater. Process. Technol.*, 2018, vol. 262, pp. 239–56.
27. H.A. Derazkola and F. Khodabakhshi: *Int. J. Adv. Manuf. Technol.*, 2019, vol. 102, pp. 4383–95.
28. G.Q. Huang, T.H. Chou, S.F. Liu, B. Xiao, J. Ju, J. Gan, T. Yang, P. Zhang, J.X. Yang, C.Y. Lu, and F.Q. Meng: *Mater. Character.*, 2023, vol. 200, 112903.
29. J. Wu, F.J. Cao, T. Sun, G.Q. Huang, M.S. Li, W.T. Hou, Z.Y. Piao, Z.K. Shen, and Y.F. Shen: *Surf. Coat. Technol.*, 2023, vol. 457, 129295.
30. A. Shahnam, F. Karimzadeh, M.A. Golozar, and S.N. Hosseini: *J. Mater. Eng. Perform.*, 2019, vol. 28, pp. 4593–4601.
31. Y. Liu, Y. Li, Q. Zhu, H. Zhang, X. Qi, J. Wang, P. Jin, and X. Zeng: *J. Magn. Alloy.*, 2021, vol. 9, pp. 499–504.
32. Y.B. Tan, X.M. Wang, M. Ma, J.X. Zhang, W.C. Liu, R.D. Fu, and S. Xiang: *Mater. Character.*, 2017, vol. 127, pp. 41–52.
33. W. Liu, Y. Shen, C. Guo, R. Ni, Y. Yan, and W. Hou: *J. Mater. Eng. Perform.*, 2019, vol. 28, pp. 4610–19.
34. B. Darras and E. Kishta: *Mater. Des.*, 2013, vol. 47, pp. 133–37.
35. F. Cao, T. Jiang, W. Hou, G. Huang, Y. Shen, Y. Ding, and P. Shu: *Mater. Chem. Phys.*, 2022, vol. 283, 126026.
36. T. Sun, Y. Shen, F. Cao, Y. Yan, R. Ni, and J. Jin: *J. Adhes. Sci. Technol.*, 2022, vol. 36, pp. 972–87.
37. T. Sun, S. Wu, Y. Shen, J. Jin, J. Lu, and T. Qin: *Trans. Indian Inst. Met.*, 2021, vol. 74, pp. 3045–61.
38. M.A. Mofid, A. Abdollah-zadeh, and F. Malek Ghaini: *Mater. Des.*, 2012, vol. 36, pp. 161–67.
39. F. Chai, D. Zhang, and Y. Li: *J. Magn. Alloy.*, 2015, vol. 3, pp. 203–09.
40. N.D. Ghetiya, K.M. Patel, and A.B. Patel: *Int. J. Adv. Manuf. Technol.*, 2015, vol. 79, pp. 1239–46.
41. S.M. Fatemi and H. Paul: *Mater. Chem. Phys.*, 2021, vol. 257, 123726.
42. A. Jamali, A. Ma, and J. Llorca: *Scr. Mater.*, 2022, vol. 207, p. 114304.
43. I. Basu and T. Al-Samman: *Acta Mater.*, 2015, vol. 96, pp. 111–32.
44. C.D. Barrett, A. Imandoust, A.L. Oppedal, K. Inal, M.A. Tschopp, and H. El Kadiri: *Acta Mater.*, 2017, vol. 128, pp. 270–83.
45. M.A. Wahid, Z.A. Khan, A.N. Siddiquee, R. Shandley, and N. Sharma: *Proc. Inst. Mech. Eng. Part B*, 2019, vol. 233, pp. 1700–10.
46. Y. Liu, Y. Li, H. Zhang, Q. Zhu, X. Qi, J. Wang, J. Wang, P. Jin, and X. Zeng: *Mater. Character.*, 2020, vol. 162, 110192.
47. Q. Shang, D.R. Ni, P. Xue, B.L. Xiao, K.S. Wang, and Z.Y. Ma: *J. Mater. Process. Technol.*, 2019, vol. 264, pp. 336–45.
48. R. Jain, S.K. Pal, and S.B. Singh: *J. Manuf. Process.*, 2016, vol. 23, pp. 278–86.
49. A. Kundu and D.P. Field: *Mater. Sci. Eng. A*, 2016, vol. 667, pp. 435–43.
50. Q.Y. Che, K.S. Wang, W. Wang, L.Y. Huang, T.Q. Li, X.P. Xi, P. Peng, and K. Qiao: *Rare Met.*, 2021, vol. 40, pp. 2552–59.
51. Z. Yan, J. Zhu, Z. Zhang, Q. Wang, and Y. Xue: *Front. Mater.*, 2022, vol. 9, pp. 1–23.
52. J. Wu, L. Jin, J. Dong, F. Wang, and S. Dong: *J. Mater. Sci. Technol.*, 2020, vol. 42, pp. 175–89.
53. K.V. Rao and C.S. Sunandana: *J. Mater. Sci.*, 2008, vol. 43, pp. 146–54.
54. N. Dixit, K.Y. Xie, K.J. Hemker, and K.T. Ramesh: *Acta Mater.*, 2015, vol. 87, pp. 56–67.
55. Z. Wu, J. Yu, Z. Zhang, H. Hu, and Z. Zhang: *JOM*, 2022, vol. 74, pp. 2566–76.
56. Z. Gao, J. Feng, Z. Wang, J. Niu, and C. Sommitsch: *Metals*, 2019, vol. 9, pp. 1–15.
57. Y.C. Lin, D.X. Wen, M.S. Chen, and X.M. Chen: *Appl. Phys. A*, 2016, vol. 122, pp. 1–16.
58. W. Hou, Y. Ding, G. Huang, N. Huda, L. Hakim, and A. Shah: *Int. J. Adv. Manuf. Technol.*, 2022, vol. 121, pp. 7661–75.
59. W. Wang, P. Han, P. Peng, T. Zhang, Q. Liu, S.N. Yuan, L.Y. Huang, H.L. Yu, K. Qiao, and K.S. Wang: *Acta Metall. Sin.*, 2020, vol. 33, pp. 43–57.
60. L. Huang, K. Wang, W. Wang, J. Yuan, K. Qiao, T. Yang, P. Peng, and T. Li: *Eng. Fail. Anal.*, 2018, vol. 92, pp. 392–404.
61. C.I. Chang, X.H. Du, and J.C. Huang: *Scr. Mater.*, 2007, vol. 57, pp. 209–12.
62. F. Chai, D. Zhang, Y. Li, and W. Zhang: *J. Mater. Sci.*, 2015, vol. 50, pp. 3212–25.
63. M. Azizieh, M. Mazaheri, Z. Balak, H. Kafashan, and H.S. Kim: *Mater. Sci. Eng. A*, 2018, vol. 712, pp. 655–62.

64. A. Fitzner, J. Palmer, B. Gardner, M. Thomas, M. Preuss, and J.Q. da Fonseca: *J. Mater. Sci.*, 2019, vol. 54, pp. 7961–74.
65. H. Yu, Y. Xin, M. Wang, and Q. Liu: *J. Mater. Sci. Technol.*, 2018, vol. 34, pp. 248–56.
66. S. Lee, Y. Park, and Y. Lee: *Mater. Sci. Eng.*, 2009, vol. 515, pp. 32–37.
67. L. Li, W. Liu, F. Qi, D. Wu, and Z. Zhang: *J. Magn. Alloy*, 2022, vol. 10, pp. 2334–53.
68. N. Hassanamraji, A.R. Eivani, and M.R. Aboutalebi: *J. Mater. Res. Technol.*, 2021, vol. 14, pp. 2998–3017.
69. I.J. Beyerlein, L. Capolungo, P.E. Marshall, R.J. McCabe, and C.N. Tome: *Philos. Mag.*, 2010, vol. 90, pp. 2161–90.
70. H.J. Liu, H.J. Zhang, Y.X. Huang, and L. Yu: *Trans. Nonferr. Met. Soc. China*, 2010, vol. 20, pp. 1387–91.
71. G. Liu, L.N. Ma, Z.D. Ma, X.S. Fu, G.B. Wei, Y. Yang, T.C. Xu, W.D. Xie, and X.D. Peng: *Acta Metall. Sin.*, 2018, vol. 31, pp. 853–64.
72. X. Liu, B.W. Zhu, C. Xie, J. Zhang, C.P. Tang, and Y.Q. Chen: *Mater. Sci. Eng. A*, 2018, vol. 733, pp. 98–107.

Publisher's Note Springer Nature remains neutral with regard to jurisdictional claims in published maps and institutional affiliations.

Springer Nature or its licensor (e.g. a society or other partner) holds exclusive rights to this article under a publishing agreement with the author(s) or other rightsholder(s); author self-archiving of the accepted manuscript version of this article is solely governed by the terms of such publishing agreement and applicable law.